

Ab initio Study of Cross-Interface Electron-Phonon Couplings in FeSe Thin Films on SrTiO₃ and BaTiO₃

Y. Wang,¹ A. Linscheid,² T. Berlijn,^{3,4} and S. Johnston¹

¹*Department of Physics and Astronomy, University of Tennessee, Knoxville, Tennessee 37996, USA*

²*Department of Physics, University of Florida, Gainesville, Florida 32611, USA*

³*Center for Nanophase Materials Sciences, Oak Ridge National Laboratory, Oak Ridge, Tennessee 37831, USA*

⁴*Computer Science and Mathematics Division, Oak Ridge National Laboratory, Oak Ridge, Tennessee 37831, USA*

(Dated: June 8, 2022)

We study the electron-phonon coupling strength near the interface of monolayer and bilayer FeSe thin films on SrTiO₃, BaTiO₃, and oxygen-vacant SrTiO₃ substrates, using *ab initio* methods. The calculated total electron-phonon coupling strength $\lambda = 0.2\text{--}0.3$ cannot account for the high $T_c \sim 70$ K observed in these systems through the conventional phonon-mediated pairing mechanism. In all of these systems, however, we find that the coupling constant of a polar oxygen branch peaks at $\mathbf{q} = 0$ with negligible coupling elsewhere, while the energy of this mode coincides with the offset energy of the replica bands measured recently by angle-resolved photoemission spectroscopy experiments. But the integrated coupling strength for this mode from our current calculations is still too small to produce the observed high T_c , even through the more efficient pairing mechanism provided by the forward scattering. We arrive at the same qualitative conclusion when considering a checkerboard antiferromagnetic configuration in the Fe layer. In light of the experimental observations of the replica band feature and the relatively high T_c of FeSe monolayers on polar substrates, our results point towards a cooperative role for the electron-phonon interaction, where the cross-interface interaction acts in conjunction with a purely electronic interaction. We also discuss a few scenarios where the coupling strength obtained here may be enhanced.

PACS numbers: 74.70.Xa, 74.20.Pq, 74.25.Kc, 74.78.-w

I. INTRODUCTION

Single-unit-cell-thick thin films of FeSe (called monolayer FeSe hereafter) grown on a SrTiO₃(001) (STO) substrate by molecular beam epitaxy (MBE)¹ have recently set a new record for the highest superconducting transition temperature T_c in iron-based superconductors (FeSC).² Typical values of T_c range between 55–65 K as measured by *in situ* scanning tunneling microscopy/spectroscopy (STM/STS),¹ angle-resolved photoemission spectroscopy (ARPES),^{3–6} *ex situ* transport measurements, and Meissner effect studies.^{7–9} Moreover, a recent *in situ* transport measurement¹⁰ found a remarkably high $T_c = 109$ K, well above the liquid nitrogen boiling point (77 K). These large values of T_c are greatly enhanced by one order of magnitude from the value of around 8 K for bulk FeSe under ambient pressure.¹¹

In general, strong magnetic interactions are believed to provide the major glue for superconducting pairing in FeSC by most researchers;^{12,13} however, the increase in T_c observed for the FeSe/STO interface has raised questions about the role of the interface. In this sense, the STO substrate is not unique as a similar high $T_c = 70\text{--}75$ K was obtained for the monolayer FeSe deposited on a ferroelectric BaTiO₃(001) (BTO) substrate.¹⁴ Similarly, lower T_c 's (around 30 K by transport measurements in Ref. 15, 60 K by ARPES in Ref. 16) were measured recently for the monolayer FeSe deposited on SrTiO₃(110) [FeSe/STO(110)] substrates.^{15,16} While the very high T_c , controllable fabrication by MBE on a variety of substrates, and low dimensionality of the monolayer FeSe

promise great practical applications, understanding the mechanism of the superconductivity will be invaluable for further enhancing the T_c or designing new high- T_c superconductors.

At present, several things are known about the influence of the substrate. First, there is a large tensile strain applied by the substrate onto the monolayer FeSe due to different lattice constants between the substrate and bulk FeSe,^{1,17} but a direct correlation between superconductivity and tensile strain seems to be unlikely.¹⁴ Interestingly, an orthorhombic distortion is observed in FeSe/STO(110), where an isotropic gap and a gap closing $T_c \sim 60$ K are measured by ARPES.¹⁶ Second, ARPES experiments reveal that the monolayer FeSe on an STO substrate is heavily electron doped such that the Fermi surface consists of only electron pockets at Brillouin zone (BZ) corner.^{3–6} It is generally believed that this electron doping is caused by oxygen vacancies in the STO surface induced by annealing of the substrate before the growth of FeSe.⁵ The large electron-doping and the resulting Fermi surface with only electron pockets directly challenge the Fermi-surface-nesting driven, purely electronic pairing mechanism.^{18,19} One way to reconcile such a scenario is by taking account of the holelike band located below the Fermi level at Γ point,^{20,21} since the band top is less than 100 meV away from the Fermi level, i.e., an “incipient” band²¹ that might fall in the low-energy cutoff of the bosons mediating pairing. The substrate, however, also influences the phononic degrees of freedom and the electron-phonon (*e-ph*) interaction, which can lead to phonon contributions to the superconductivity.

For example, the STO substrate has a stabilizing effect for the shearing motion of the FeSe layer that serves to enhance the total coupling to the Fe and Se derived phonon modes.²² Another intriguing possibility is the presence of cross-interface coupling between the FeSe layer and the substrate.^{6,23} Evidence for the latter possibility has been inferred from recent ARPES experiments (Ref. 6 for FeSe/STO and later Ref. 14 for FeSe/BTO), which observed replica bands 100 meV below the main electronic bands.^{6,14} These replica bands were interpreted as shake-off states produced by the coupling between the FeSe electrons and an oxygen optical phonon branch in the substrate.^{6,23}

The shape and intensity of the replica bands have been used to infer a strong coupling between the oxygen optical phonons and the Fe 3*d* electrons that is strongly peaked for small momentum transfers (forward scattering).⁶ This is a significant experimental result, as such coupling can produce substantial enhancements in the total T_c of FeSe/STO, even in unconventional channels where phonons are not expected to play an essential role.^{6,24,25} Moreover, this cross-interface coupling provides a natural framework for understanding the T_c enhancement in the FeSe/BTO system.¹⁴ This momentum structure has been qualitatively confirmed by recent *ab initio* calculations for the interface *e-ph* coupling.²⁶ However, in light of the sharpness of the replica bands, the q -resolution in Ref. 26 is not in line with the sharpness of the coupling in momentum space that is necessary to explain this experiment.

Motivated by this, we investigate the *e-ph* coupling for films of FeSe on different oxide substrates using *ab initio* methods. We first determine the phonon dispersion relations, the Eliashberg spectral function $\alpha^2 F(\omega)$, and the total coupling strength λ for the following four systems: case (a), a monolayer of FeSe on a SrTiO₃ substrate (FeSe/STO); case (b), a monolayer of FeSe on an oxygen-vacant SrTiO₃ substrate with a (1 × 2) reconstruction (FeSe/STO1x2); case (c), a bilayer of FeSe on a SrTiO₃ substrate (2L-FeSe/STO); and case (d), a monolayer of FeSe on a BaTiO₃ substrate (FeSe/BTO). Next, we study the momentum dependent coupling strength $\lambda_{\nu\mathbf{q}}$ for various phonon branches ν and specifically focus on the top-most branch, an oxygen phonon branch whose energy coincides with the offset energy of the replica bands measured by ARPES. Using a similar q sampling, we find all four systems have a comparable total coupling strength $\lambda = 0.2\text{--}0.3$, consistent with the calculation result for the FeSe/STO in Ref. 26. Furthermore, for all systems and substrates explored, we investigate the momentum dependence of the coupling in Sec. III B by computing the matrix elements $g(\mathbf{k}, \mathbf{q})$ at a few q -points at and very close to Γ . While, as expected from the experiments, we find a large coupling at $\mathbf{q} = 0$ and negligible couplings at $\mathbf{q} \neq 0$ in our calculations. We find, however, that the integrated coupling strength is insufficient to account for the high T_c observed in the monolayer FeSe/STO system on its own. This points to a cooperative role played by

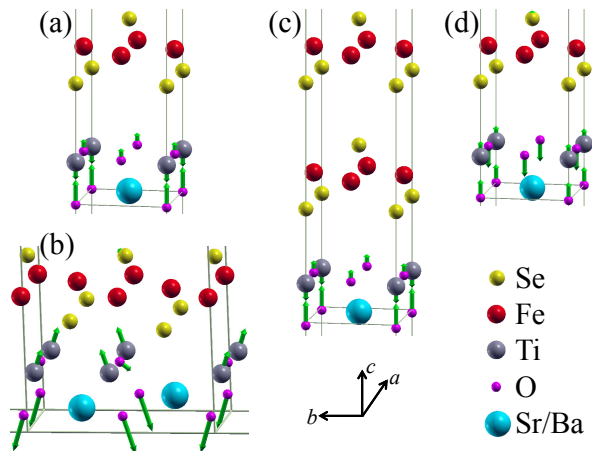


FIG. 1. (color online). Relaxed crystal structures for FeSe on TiO₂-terminated SrTiO₃ [BaTiO₃ in (d)]. We consider monolayers of FeSe in (a), (b) and (d) and a bilayer of FeSe in (c). The arrows indicate the direction and amplitude of the atomic displacements associated with mode $\nu = 27$ (a), $\nu = 48$ (b), $\nu = 39$ (c), and $\nu = 24$ (d) (defined in text). The displacements are vectors $\mathbf{u}_{s,\nu}(\mathbf{q})$ with components $u_{s,\nu}^\alpha(\mathbf{q}) = \varepsilon_{s,\nu}^\alpha(\mathbf{q})/\sqrt{M_s}$, where $\varepsilon_{s,\nu}^\alpha(\mathbf{q})$ are eigenvectors defined in the text. All structures are in a slab geometry where the lattice is repeated in the *ab*-plane and separated by a vacuum layer before being repeated in the *c*-direction. The vacuum layer is not shown here.

the cross-interface coupling. We discuss in the end a few scenarios where the coupling to this branch may be enhanced and the necessity of a cooperative pairing mechanism between the forward scattering *e-ph* interaction and a purely electronic interaction based on the current results.

II. MODEL AND METHOD

The four crystal structures considered in this work, each in a slab geometry, are shown in Fig. 1. In all cases the substrates are one unit cell thick, and terminated at the TiO₂ surface. We set $a = 3.905 \text{ \AA}$ as the in-plane lattice constant for both the substrate and FeSe layer and place a vacuum layer around 12 \AA in height above the FeSe layers before the structure is repeated in the *c*-direction. All structures are relaxed until a force smaller than 0.2 meV/ \AA is found on each atom. The relaxed structures for all cases are shown in Fig. 1. In Fig. 1(b), the oxygen atoms in the Ti-O chain along *b*-direction have been removed, resulting in the more stable (1 × 2) reconstructed structure, similar to that inferred from several experiments^{1,27} and a theoretical calculation.²⁸ Thus, the lattice constant in the *b*-direction is doubled $b = 2a$ in case (b).

The electronic structure calculations are based on density functional theory (DFT) as implemented in Quantum ESPRESSO package.²⁹ The exchange-correlation func-

tional was taken in the generalized gradient approximation (GGA) of Perdew-Burke-Ernzerhof (PBE) type³⁰ within a plane-wave pseudopotential representation. We choose an energy cutoff of 40 Ry (50 Ry) for plane-waves and 480 Ry (700 Ry) for charge densities (the higher energy cutoffs are for oxygen-vacant FeSe/STO1x2). A $16 \times 16 \times 1$ ($16 \times 8 \times 1$ for FeSe/STO1x2) Monkhorst-Pack k -grid is used for BZ summations in the DFT calculations. We have checked the computation results with local-density approximation (LDA) functional, $32 \times 32 \times 1$ k -grid sampling, or higher energy cutoffs and found no qualitative changes to our conclusions.

The dynamical properties of the lattice, including dynamical matrices, phonon dispersions, phonon density of states (PDOS), and e - ph coupling matrix elements and coupling strengths, are calculated with the density-functional perturbation theory³¹ (DFPT) implemented in Quantum ESPRESSO. The dynamical matrices are calculated on a $4 \times 4 \times 1$ q -grid ($4 \times 2 \times 1$ for FeSe/STO1x2) and then Fourier transformed to force constants in real space. The ν -th phonon mode of frequency $\omega_{\mathbf{q}\nu}$ at any wavevector \mathbf{q} are then calculated using the Fourier interpolation of the dynamical matrices through the force constants, which is a standard technique.^{31,32}

The e - ph coupling function matrix elements are

$$g_\nu(i\mathbf{k}, j\mathbf{k}') = \left(\frac{\hbar}{2\omega_{\nu\mathbf{q}}} \right)^{1/2} \langle \psi_{i\mathbf{k}} | \Delta V_{\text{SCF}}(\nu\mathbf{q}) | \psi_{j\mathbf{k}'} \rangle, \quad (1)$$

where $\mathbf{q} = \mathbf{k}' - \mathbf{k}$, $|\psi_{i\mathbf{k}}\rangle$ is the single-particle Bloch state characterized by wave vector \mathbf{k} and band index i (here we explicitly write out the band index i instead of suppressing it in \mathbf{k}), and

$$\Delta V_{\text{SCF}}(\nu\mathbf{q}) = \sum_{\mathbf{R}_l} \frac{e^{i\mathbf{q}\cdot\mathbf{R}_l}}{\sqrt{N}} \sum_{s,\alpha} \frac{1}{\sqrt{M_s}} \frac{\partial V_{\text{SCF}}}{\partial \xi_s^\alpha} \varepsilon_{s,\nu}^\alpha(\mathbf{q}), \quad (2)$$

is the self-consistent first order variation of Kohn-Sham potential due to the small displacement ξ_s^α of atom s in the direction α of cartesian coordinates. Here, $\varepsilon_{s,\nu}^\alpha(\mathbf{q})$ is the eigenvector of the phonon mode with wave vector \mathbf{q} , branch index ν , and frequency $\omega_{\nu\mathbf{q}}$; N is the number of unit cells in the crystal; M_s is the mass of atom $s \in \{1, \dots, S\}$ in the unit cell $\mathbf{R}_l \in \{\mathbf{R}_1, \dots, \mathbf{R}_N\}$; and $\alpha \in \{1, 2, 3\}$ is the cartesian coordinate index.

The dimensionless momentum-resolved coupling strength is defined as

$$\lambda_\nu(i\mathbf{k}, j\mathbf{k} + \mathbf{q}) = 2N_{\text{F}} |g_\nu(i\mathbf{k}, j\mathbf{k} + \mathbf{q})|^2 / \omega_{\nu\mathbf{q}}, \quad (3)$$

where N_{F} is the electronic density of states (DOS) per spin per unit cell at the Fermi level. The dimensionless ‘‘monochromatic’’ coupling strength is defined as

$$\lambda_{\nu\mathbf{q}} = \frac{1}{N_{\text{F}}^2 N} \sum_{\mathbf{k}, i, j} \lambda_\nu(i\mathbf{k}, j\mathbf{k} + \mathbf{q}) \delta(\epsilon_{i\mathbf{k}}) \delta(\epsilon_{j\mathbf{k}+\mathbf{q}}), \quad (4)$$

and the total dimensionless e - ph coupling constant

(EPC) is defined as

$$\lambda = \frac{1}{N} \sum_{\mathbf{q}, \nu} \lambda_{\nu\mathbf{q}}. \quad (5)$$

For the discussion below, denote $\lambda_{\mathbf{q}} = \sum_{\nu} \lambda_{\nu\mathbf{q}}$ and $\lambda_\nu = \frac{1}{N} \sum_{\mathbf{q}} \lambda_{\nu\mathbf{q}}$. The Eliashberg spectral function is

$$\alpha^2 F(\omega) = \frac{1}{2N} \sum_{\mathbf{q}, \nu} \lambda_{\mathbf{q}\nu} \omega_{\mathbf{q}\nu} \delta(\omega - \omega_{\mathbf{q}\nu}), \quad (6)$$

the frequency-dependent EPC is

$$\lambda(\omega) = 2 \int_0^\omega \frac{\alpha^2 F(\omega')}{\omega'} d\omega', \quad (7)$$

and the total EPC is $\lambda = \lambda(\infty)$. Last, the phonon density of states (PDOS) is $D(\omega) = \frac{1}{N} \sum_{\mathbf{q}, \nu} \delta(\omega - \omega_{\mathbf{q}\nu})$.

Before continuing, it should be noted that Eq. (4), widely used in *ab initio* studies, is an approximate formula because the phonon energy transfer $\omega_{\nu\mathbf{q}}$ has been dropped in one of delta functions in what should be an energy conserved scattering process (the so called double delta-function approximation). If $\omega_{\nu\mathbf{q}}$ is not small, the approximate result from Eq. (4) will deviate from the more accurate formula, especially for optical phonon with a finite coupling at $\mathbf{q} = 0$.³³ If only the total EPC is needed and the $\mathbf{q} = 0$ is assumed to have negligible weight *a priori*, one can apply Eq. (4) but the convergence of total EPC on the q -grid needs to be checked. Because of this, a dense q -grid is necessary to accurately sum over \mathbf{q} in Eq. (5). For our systems it is impractical to directly calculate the coupling matrix elements on every q -point in such a dense q -grid. Various interpolation techniques are available to circumvent this difficulty, such as Fourier interpolation by maximally localized Wannier functions^{34–36} or by using the auxiliary phonon linewidths,³⁷ and an improved tetrahedron method.³⁸ We use the method in Ref. 37 (as it is already implemented in Quantum ESPRESSO package) to compute $\lambda_{\mathbf{q}}$ on a dense $24 \times 24 \times 1$ q -grid that is needed for the summation in Eq. (5). A $32 \times 32 \times 1$ k -grid and a broadening $\eta = 0.005$ Ry is used in Eq. (4). Note, however, none of the interpolation techniques mentioned above can properly treat the matrix elements with long spatial decay in real space, or with a strong peak near $\mathbf{q} = 0$ in momentum space.^{39,40} This is most likely to be the case where $\mathbf{q} = 0$ weight is not negligible. We will come back to this comment again below.

III. RESULTS AND ANALYSIS

A. Band Structure, Phonon Dispersion and e - ph Coupling

Fig. 2 shows the calculated electronic band structure and DOS for the corresponding four cases defined before.

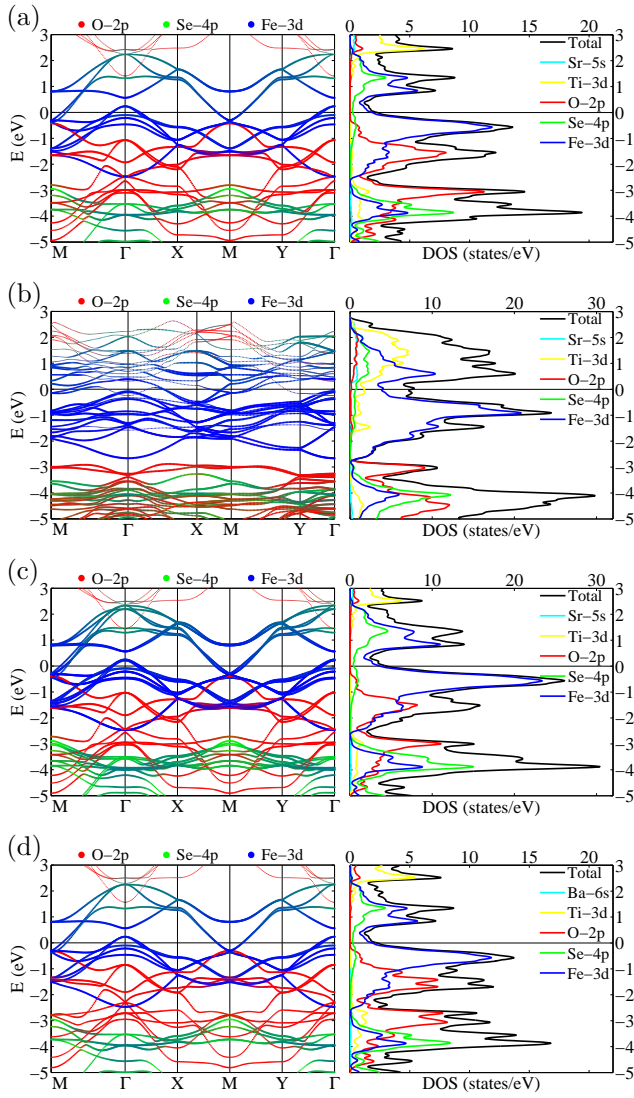


FIG. 2. (color online). (a) FeSe/STO, (b) oxygen-vacant FeSe/STO1x2, (c) 2L-FeSe/STO, (d) FeSe/BTO. Left: band structure. The RGB values of the dots are determined by the orbital weight: red for O atoms, green for Se atoms, and blue for Fe atoms. The size of the dots is proportional to the sum of the orbital weight considered. Right: total and projected DOS (summed for two spin components).

The results in panel Fig. 2(a) and Fig. 2(b) agree well with prior calculations.^{26,28} The bands near the Fermi level are mainly Fe *d* bands. Fig. 2(a) shows a peak in the O-*p* density of states around -2 eV which however is absent in the presence of oxygen vacancies as shown in Fig. 2(b). The similarity of band structure in panel Fig. 2(a) and Fig. 2(d) indicates that there is only small difference between STO and BTO substrate in electronic structure; panel Fig. 2(c) shows the second FeSe layer simply doubles the Fe *d* states near the Fermi level. In panel Fig. 2(b), however, O-vacancy strongly changes the band structure by electron doping the system and removing the Fe *d* hole pockets at Γ . In addition, there is an

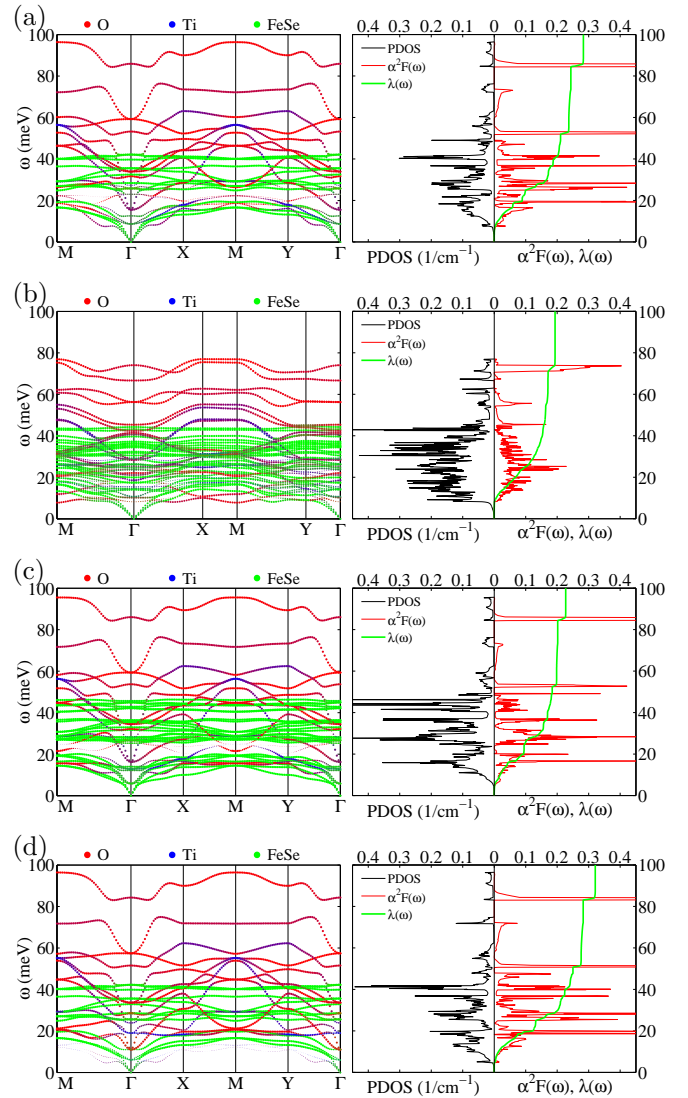


FIG. 3. (color online). (a) FeSe/STO, (b) oxygen-vacant FeSe/STO1x2, (c) 2L-FeSe/STO, (d) FeSe/BTO. Left: phonon dispersion. The RGB values of the dots are determined by the eigenvector $|\varepsilon_{s,\nu}^{\alpha}(\mathbf{q})|^2$ of the mode $\omega_{\nu\mathbf{q}}$: red for O atoms, blue for Ti atoms, and green for both Fe and Se atoms. The size of the dots is proportional to the sum of the eigenvector components considered. Right: phonon density of states (black line), Eliashberg spectral function $\alpha^2F(\omega)$ [red (gray) line] and *e-ph* coupling $\lambda(\omega)$ [green (light gray) line].

increment of Ti *d* states near Fermi level and a quite large Ti *d* electron pocket around Γ .

Fig. 3 shows the phonon dispersion relations, the PDOS, and the EPC $\lambda = \lambda(\infty)$. One important result is that the topmost phonon branch (denoted as mode ν below)—a set of oxygen polar modes—has an energy around 80–100 meV in each case. The dispersion of this branch softens to an energy below 80 meV in case (b) for the system with O-vacant substrate, which can be explained by the charge transfer between the STO substrate and FeSe monolayer.⁴¹ The phonon energy of this

oxygen phonon is consistent with the inferred ~ 80 meV phonon that causes the replica bands seen in ARPES experiment.⁶ The displacement pattern of the $\mathbf{q} = 0$ mode is shown in Fig. 1 for each case. These vibrations can induce excess z -directional dipole moments situated at a plane near the surface, as suggested in Refs. 6 and 23, and result in an e - ph coupling between the substrate phonons and the FeSe electrons. Indeed, we find that this mode alone contributes a sizeable amount to the total e - ph coupling strength and has a relatively flat dispersion, resulting in a sharp peak in the Eliashberg spectral function $\alpha^2F(\omega)$ (right panels in Fig. 3). Our result shows this peak is not unique to FeSe/STO system,²⁶ but also exists in BTO and/or O-vacant STO substrates. Further investigation, presented in the next section, shows that most of the coupling to this oxygen mode is due to the intraband matrix elements of zero momentum transfer.

We stress that there are two factors that contribute to an overestimation of λ . First, the standard interpolation techniques do not work properly when the coupling is strongly peaked at $\mathbf{q} = 0$, as they tend to overestimate the width of the peak in momentum space. Second, this mode has a finite contribution at $\mathbf{q} = 0$, which will be strongly boosted by the double delta-function approximation. The net result is that the contribution of this coupling to total EPC $\lambda(\infty)$ in Fig. 3 is overestimated and should be considered as upper limit of the EPC in these systems. For the same reasons, the calculated coupling strengths and widths in q -space in Ref. 26 are overestimated.

Before we introduce a proper way to characterize the q -dependence of the e - ph interaction without resorting to the double delta-function approximation, we compare some other aspects of the four cases. First, from the color-coded dispersion relations, we see that the phonon modes of FeSe layer are all below 50 meV. We again find the two systems—(a) FeSe/STO and (d) FeSe/BTO—have a similar phonon spectrum, PDOS, and EPC. (One difference is that the Ba atom has a large weight in the eigenvector of the lowest modes in panel (d) as the weights plotted for O, Ti, and FeSe are small.) Comparing Fig. 3(a) and Fig. 3(c), we find that the second layer of FeSe doesn't alter the existing phonon modes too much and seems to only add more phonon modes below 50 meV. Nevertheless, the corresponding e - ph coupling is smaller. Finally, the total EPC for case (b) is also smaller than the other cases. We summarize the quantitative results in Table I. In the table, we define $\omega_{\text{in}} = \exp\left(\frac{2}{\lambda} \int d\omega \omega^{-1} \alpha^2 F(\omega) \ln \omega\right)$ and $\int_0^{\omega_D} D(\omega) d\omega = 3S/2$, where $D(\omega)$ is the phonon DOS, $3S$ is total number of phonon modes, and ω_D is the Debye energy defined here.

B. Momentum Dependence of e - ph Coupling

When we consider the momentum \mathbf{q} dependence of the e - ph coupling as defined in Eq. (4), we find a few disadvantages that are related to the double delta-function

TABLE I. Numerical values of the calculation result for all cases: (a) FeSe/STO, (b) oxygen-vacant FeSe/STO1x2, (c) 2L-FeSe/STO, and (d) FeSe/BTO. The DOS N_F is per spin per unit cell. The particular oxygen mode is $\nu = 27$ (a, d), $\nu = 48$ (b), and $\nu = 39$ (c).

Case	λ	λ_ν	N_F (states/eV)	ω_{in} (meV)	ω_D (meV)
(a)	0.283	0.040	1.00	29.8	31.0
(b)	0.193	0.022	3.67	25.9	27.8
(c)	0.227	0.025	2.02	25.9	31.1
(d)	0.321	0.038	1.00	27.7	30.0

approximation we mentioned before. First, the two delta functions in Eq. (4) require a large k -point sampling to achieve an accurate result, so the k -summed coupling strength is sensitive to k -grid and Fermi surface broadening. Second, the nesting property of the Fermi surface, i.e., the phase space for scattering on the Fermi surface, will strongly affect the value of the two delta functions and make it difficult to infer or compare the magnitude of the coupling matrix elements $|g_\nu(i\mathbf{k}, j\mathbf{k} + \mathbf{q})|$ or $\lambda_\nu(i\mathbf{k}, j\mathbf{k} + \mathbf{q})$ from the calculated $\lambda_{\nu\mathbf{q}}$.

In order to circumvent these difficulties, we define a Fermi surface average $\langle \lambda_{\nu\mathbf{q}} \rangle$ by separating the nesting property and the matrix elements in $\lambda_{\nu\mathbf{q}}$. We begin with the phonon linewidth^{34,42}

$$\gamma_{\nu\mathbf{q}} = -\text{Im} \Pi_{\nu\mathbf{q}} = \frac{2\pi\omega_{\nu\mathbf{q}}}{N} \sum_{\mathbf{k}, ij} |g_\nu(i\mathbf{k}, j\mathbf{k} + \mathbf{q})|^2 \times \frac{f(\epsilon_{i\mathbf{k}}) - f(\epsilon_{i\mathbf{k}} + \omega_{\nu\mathbf{q}})}{\omega_{\nu\mathbf{q}}} \delta(\epsilon_{j\mathbf{k} + \mathbf{q}} - \epsilon_{i\mathbf{k}} - \omega_{\nu\mathbf{q}}), \quad (8)$$

where $\Pi_{\nu\mathbf{q}}$ is the phonon self-energy and $f(x) = 1/[\exp(x/T) + 1]$ is the Fermi distribution function. We have replaced $\epsilon_{j\mathbf{k} + \mathbf{q}}$ in the second Fermi distribution with $\epsilon_{i\mathbf{k}} + \omega_{\nu\mathbf{q}}$. The ‘‘monochromatic’’ coupling strength is then given by

$$\tilde{\lambda}_{\nu\mathbf{q}} = \frac{\gamma_{\nu\mathbf{q}}}{\pi N_F \omega_{\nu\mathbf{q}}^2}. \quad (9)$$

Only when $\omega_{\nu\mathbf{q}}$ is much smaller than the temperature broadening, do we have $\tilde{\lambda}_{\nu\mathbf{q}} \approx \lambda_{\nu\mathbf{q}}$. Next, we define the nesting function^{43,44}

$$\tilde{\xi}(\mathbf{q}, \omega_{\nu\mathbf{q}}) = \frac{1}{N} \sum_{\mathbf{k}, ij} \frac{f(\epsilon_{i\mathbf{k}}) - f(\epsilon_{i\mathbf{k}} + \omega_{\nu\mathbf{q}})}{\omega_{\nu\mathbf{q}}} \times \delta(\epsilon_{j\mathbf{k} + \mathbf{q}} - \epsilon_{i\mathbf{k}} - \omega_{\nu\mathbf{q}}), \quad (10)$$

and the approximate form

$$\xi(\mathbf{q}) = \frac{1}{N} \sum_{\mathbf{k}, ij} \delta(\epsilon_{i\mathbf{k}}) \delta(\epsilon_{j\mathbf{k} + \mathbf{q}}). \quad (11)$$

Some of the properties of $\xi(\mathbf{q})$ are discussed in Ref 44. It's easy to see $N^{-1} \sum_{\mathbf{q}} \xi(\mathbf{q}) = N_F^2$. Finally, we define

the new k -averaged coupling constant as

$$\langle \lambda_{\nu\mathbf{q}} \rangle = \frac{N_F^2 \lambda_{\nu\mathbf{q}}}{\xi(\mathbf{q})}, \quad (12)$$

$$\langle \tilde{\lambda}_{\nu\mathbf{q}} \rangle = \frac{N_F^2 \tilde{\lambda}_{\nu\mathbf{q}}}{\tilde{\xi}(\mathbf{q}, \omega_{\nu\mathbf{q}})}. \quad (13)$$

These coupling constants characterizes the \mathbf{q} dependence of the e - ph matrix element $|g_\nu(i\mathbf{k}, j\mathbf{k} + \mathbf{q})|^2$, independent of the Fermi surface shape and the size of phase space for scattering processes determined by the Fermi surface shape. The tilde ($\tilde{}$) indicates including the phonon frequency in one of the delta function, while the non-tilde notation means the double delta-function approximation is applied.

In Fig. 4(a), we plot the calculated $\lambda_{\nu\mathbf{q}}$ and the mode-summed $\lambda_{\mathbf{q}} = \sum_\nu \lambda_{\nu\mathbf{q}}$, using a denser $8 \times 8 \times 1$ q -grid to illustrate the momentum dependence of the interaction. In Fig. 4(b), we plot $\langle \lambda_{\nu\mathbf{q}} \rangle$ and $\langle \lambda_{\mathbf{q}} \rangle$, which were computed using the e - ph coupling matrix elements $g_\nu(i\mathbf{k}, j\mathbf{k} + \mathbf{q})$ directly calculated by DFPT at each momentum \mathbf{q} with a $16 \times 16 \times 1$ k -grid and then interpolated to a $64 \times 64 \times 1$ k -grid for the k -sum. Only the bands i, j crossing the Fermi level are included in the sum. The delta function is approximated by a Gaussian $\delta(x) = \frac{1}{\sqrt{\pi}\eta} e^{-x^2/\eta^2}$. The temperature broadening in the Fermi distribution function and Gaussian broadening in the delta function are both set to 0.005 Ry.

In Fig. 4(a), we see the mode-summed couplings have a very strong q -dependence, whether we use exact Eq. (9) or approximate Eq. (4); however, in Fig. 4(b), the mode-summed couplings all reach a comparable level across the high symmetry path when the size of phase space for scattering processes is separated by the normalization of the nesting function. This indicates that the total e - ph interaction, averaged over all modes, is fairly momentum independent. In contrast, $\langle \lambda_{\nu\mathbf{q}} \rangle$ (and $\langle \tilde{\lambda}_{\nu\mathbf{q}} \rangle$) of the oxygen mode $\nu = 27$ (for FeSe/STO system), is still peaked at $\mathbf{q} = 0$. (Mode $\nu = 24$, which corresponds to the optical oxygen branch at ~ 60 meV, shows similar behavior but is not plotted.) Since $\langle \lambda_{\nu\mathbf{q}} \rangle$ truly reflects the magnitude the matrix elements near the Fermi surface, the matrix elements must also peak at $\mathbf{q} = 0$ and decay very fast away from it.

We can verify this in Fig. 5, where we plot $\langle \lambda_{\nu\mathbf{q}} \rangle$ and the relevant matrix elements at a few selected q -points very close to $\mathbf{q} = 0$. [We calculate $q = (0, 0, 0)$ and $(0, \pi/64, 0)$ for case (a) and (d); $q = (0, 0, 0)$ and $(0, \pi/16, 0)$ for case (b); but only $q = (0, 0, 0)$ for case (c) because of the difficulty of convergence in case (c) for q very close Γ point.] Here, results are again shown for the topmost phonon mode of each case that we considered. Note, $\langle \lambda_{\nu\mathbf{q}} \rangle$ is the average of corresponding matrix elements (insets in Fig. 5) summed over different bands; by definition only the matrix elements near the Fermi surface contribute to the average, and the size of the phase space for the scattering processes doesn't affect $\langle \lambda_{\nu\mathbf{q}} \rangle$ because it is normalized with respect to the nest-

ing function. Although it is consistent with values on the coarse q -grid shown in Fig. 4, the matrix elements decays surprisingly fast away from $\mathbf{q} = 0$. The estimated peak width is smaller than $\pi/64$, as shown by the bar graph of $\langle \lambda_{\nu\mathbf{q}} \rangle$. $\langle \tilde{\lambda}_{\nu\mathbf{q}} \rangle$ is similar. This result shows that all four cases which we have considered here have a non-zero q -dependent e - ph coupling with the topmost oxygen optical phonons, and that this interaction is strongly peaked at small momentum transfers. This result also demonstrates that the width of this interaction in momentum space is much narrower than the one inferred in Ref. 26 with the use of the double-delta function approximation and problematic interpolation methods.

We have cross-checked the existence of the striking difference between coupling matrix elements at $\mathbf{q} = 0$ and $\mathbf{q} \neq 0$ and found that it is a consistent result, appearing when we use LDA, PBE, and PBEsol types of exchange-correlation potentials in both norm-conserving and ultrasoft pseudopotential up to $\mathbf{q} = (q_x, 0, 0)$ with q_x as low as $\frac{1}{200} \frac{2\pi}{a}$.

IV. DISCUSSION

$\langle \lambda_{\mathbf{q}} \rangle$ at $\mathbf{q} = 0$ shown in Fig. 4(b) indicates it has a sizable contribution to the total EPC λ . The approximate nesting function is also overestimated at $\mathbf{q} = 0$;⁴⁵ this is why $\lambda_{\mathbf{q}}$ is so large in Fig. 4(a). Due to the concurrence of these two effects, the calculated total $\lambda = N^{-1} \sum_{\mathbf{q}} \lambda_{\mathbf{q}} = N^{-1} \sum_{\mathbf{q}} \langle \lambda_{\mathbf{q}} \rangle N_F^{-2} \xi(\mathbf{q})$ could also be overestimated, depending on factors such as the density of the q -grid and size of the broadening. Since in all the interpolation techniques mentioned before, the coupling at $\mathbf{q} = 0$ is extrapolated to a finite region, it is important to resolve this region in the initial matrix elements by direct calculation as we have shown in Fig. 5. We have indeed found the calculated λ for a $8 \times 8 \times 1$ q -grid is smaller than that listed in Table I for a $4 \times 4 \times 1$ q -grid. In either case, the calculated total e - ph coupling strength $\lambda = 0.2$ – 0.3 for all four systems we have considered cannot account for the high $T_c \sim 70$ K observed experimentally through the conventional phonon mediated pairing mechanism.

On the other hand, ARPES experiments^{6,14} found replica bands in the electronic structure in these systems, suggesting a strong e - ph coupling to phonons with mode energy ~ 100 meV.^{6,23} We have also found the suggested oxygen mode in our calculations for FeSe on STO or BTO substrates. More importantly, as shown in Fig. 4 and Fig. 5, all of these systems have a sharp peak and a non-zero coupling strength near $\mathbf{q} = 0$, i.e. they favor forward scattering process. The study in Ref. 24 suggests that the coupling to forward scattering process results in a T_c that depends linearly on the coupling constant, where an estimated coupling strength ~ 0.15 – 0.2 for the single mode alone can account for the total $T_c \sim 70$ K if the Coulomb pseudopotential μ^* is neglected. Therefore, the T_c enhancement due to this oxygen mode can

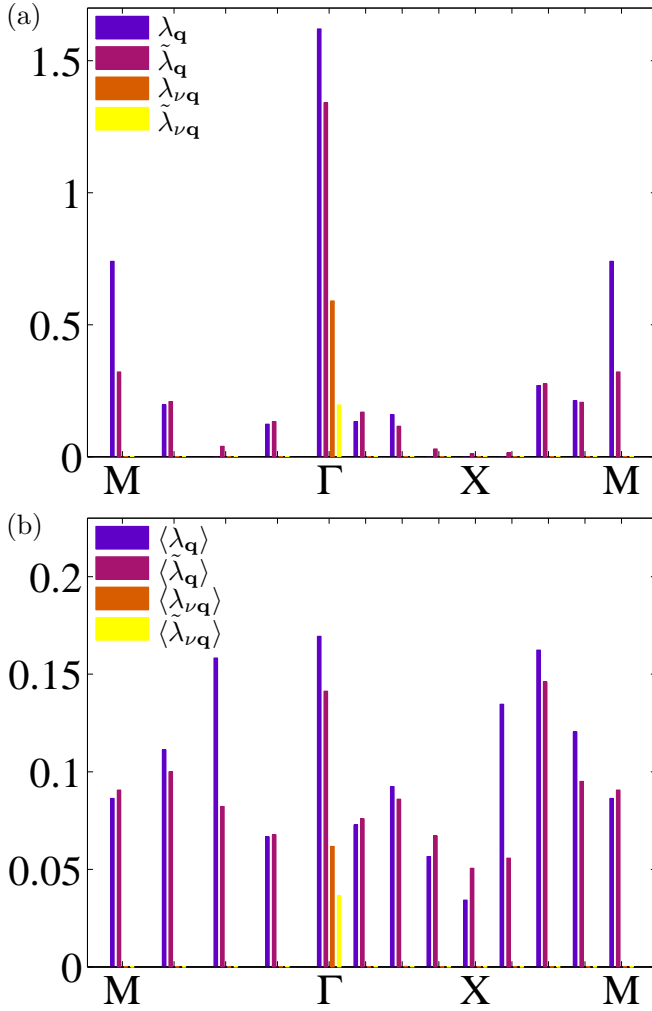


FIG. 4. (color online). The q -dependence of the e - ph coupling strength $\lambda_{\mathbf{q}}$ for FeSe/STO system. $\lambda_{\nu\mathbf{q}}$ for topmost mode $\nu = 27$ is also shown. (a) Coupling strength calculated with approximated (λ) and exact formula ($\tilde{\lambda}$). (b) Averaged coupling strength, i.e., coupling strength in (a) normalized by the corresponding nesting function.

be much larger than that expected from the conventional phonon mediated pairing mechanism. However, the coupling strength we obtain here is still too small to account for the full T_c , even when we consider the more effective pairing produced by the strong forward scattering nature of the interaction.

At this time there are a number of factors that could provide a satisfactory explanation for this discrepancy. The first is that the e - ph coupling can be enhanced when the correlations⁴⁶ or magnetic structure²⁶ are considered. In Fig. 6, we plot $\langle \lambda_{\nu\mathbf{q}} \rangle$ (summed for two spins) and the spin-dependent matrix elements from the calculation for FeSe/STO with a checkerboard antiferromagnetic (cAFM) spin configuration [denoted as the case (e)]. The electronic structure (not shown) and the enhanced total e - ph coupling constant λ are consistent with the previous calculation for FeSe/STO case;²⁶ however, $\langle \lambda_{\nu\mathbf{q}} \rangle$ for

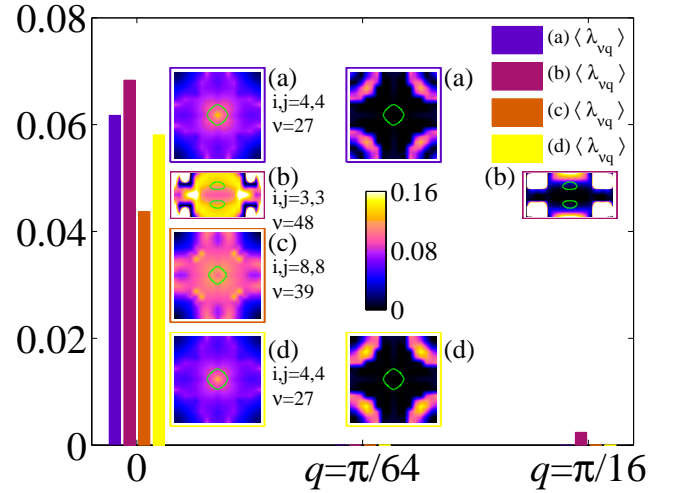


FIG. 5. (color online). The coupling strength $\langle \lambda_{\nu\mathbf{q}} \rangle$ by averaging the matrix elements (bar graph) and intraband coupling matrix elements $\lambda_{\nu}(i\mathbf{k}, j\mathbf{k} + \mathbf{q})$ in the first Brillouin zone (the rectangular inset panels) for a few q -points near $\mathbf{q} = 0$ for four cases: (a) FeSe/STO, (b) oxygen-vacant FeSe/STO1x2, (c) 2L-FeSe/STO, and (d) FeSe/BTO. Here, $\mathbf{q} = (0, q, 0) \frac{1}{a}$ and mode ν is the topmost mode in the dispersion for each case. Only one pair of (i, j) bands is shown for each case. The corners of each inset are Γ points and the center M point. The magnitude of the matrix elements is indicated by the colorbar with darker color for lower value and brighter color for higher value (any out-of-limit value is indicated by black or white). The green solid line in the inset panels is the electron pocket for the corresponding band. The matrix elements plotted in the inset panel is multiplied by 400 at $q_y = \pi/64$ and by 10 at $q_y = \pi/16$.

topmost oxygen branch decays at least as fast as in the other cases we have shown and therefore the integrated coupling for this branch is still quite small, albeit a large enhancement at $\mathbf{q} = 0$. Furthermore, there are indications that strong electronic correlations can renormalize the e - ph coupling preferentially at small momentum transfers.^{46,47} In order to address this possibility extensions beyond DFT are likely required.^{22,25} Another possibility is that vertex corrections to the e - ph interaction, which were neglected in Ref. 24, may need to be included since they can enhance T_c in the perturbative regime when the e - ph interaction is peaked at small momentum transfers.⁴⁸⁻⁵⁰ Our DFT results hint that FeSe/STO is in this regime providing that a finite integrated coupling strength from the forward-focused coupling of the oxygen mode can be obtained with an improved method.

Another possible explanation is that the ferroelectric substrate and the two-dimensionality of our system needs a more careful treatment that is beyond the current standard DFPT routines.^{39,40,51} Furthermore, the exact structure of the terminating layer of the substrate has yet to be determined. One recent experiment⁵² found the top two layers of the STO substrate (prepared by Se etching) are two adjacent TiO_2 layers. If oxygen vi-

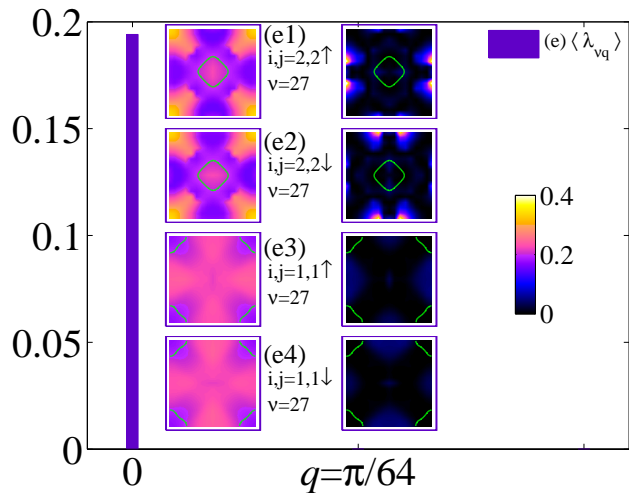


FIG. 6. (color online). The coupling strength $\langle \lambda_{\nu \mathbf{q}} \rangle$ by averaging the matrix elements (bar graph) and intraband coupling matrix elements $\lambda_{\nu}(i\mathbf{k}, j\mathbf{k} + \mathbf{q})$ in the first Brillouin zone (the inset panels) for two q -points near $\mathbf{q} = 0$ for cAFM FeSe/STO. Here, $\mathbf{q} = (0, q, 0)\frac{1}{a}$ and mode ν is the topmost mode in the dispersion. (e1) and (e2) are for the electron pocket at M for spin-up and spin-down component, respectively. (e3) and (e4) are for the hole pocket at Γ for spin-up and spin-down component, respectively. The corners of each inset panel are Γ points and the center M point. The green solid line in the inset panels is the Fermi pocket for the corresponding band. The matrix elements plotted in the inset panel is multiplied by 2000 at $q_y = \pi/64$.

brations in both layers contribute to the coupling to the d electron in FeSe layer, a stronger coupling strength is expected.

Finally, the unconventional channel of electronic pairing mechanism can play an equal, if not larger, role in the high T_c in monolayer FeSe/STO or FeSe/BTO systems. There is growing experimental evidence for this scenario. For example, the observation of superconductivity with $T_c \sim 40$ K by field-effect^{53–55} and potassium doping/surface coating^{56,57} on FeSe thin films supports this conclusion by indicating the action of an unconventional pairing mechanism. However, without the STO or BTO substrates, the T_c does not reach the value ~ 70 K, as shown by the experiments on potassium surface coating on bulk FeSe crystal.^{58,59} The presence of an electronic pairing mechanism can also explain the fact that

the bilayer FeSe/STO shows similar phonon spectrum and e - ph coupling strength, but doesn't superconduct in reality. Since the forward scattering pairing are mainly intraband in nature, it can work in conjunction with the unconventional pairing mechanism in most instances and explain the high T_c observed in the monolayer FeSe systems with the cooperative pairing mechanism.

V. CONCLUSIONS

We have calculated the phonon spectrum and e - ph coupling strength for a monolayer and bilayer of FeSe on a pristine STO or BTO substrates or on an O-vacant STO substrate. We have found an interfacial 80–100 meV ferroelectric oxygen phonon branch couples to Fe d electrons in all model structures. The energy of this mode coincides with the offset of the replica bands measured in ARPES and the coupling matrix elements has a sharp peak in q -space, preferring forward scattering process. Although the calculated coupling strength is insufficient to explain the high T_c observed by ARPES experiments through phonon-mediated pairing mechanism for either the momentum independent coupling or the forward scattering coupling, our results suggest that the inferred coupling enhances T_c through a cooperative mechanism with an unconventional pairing channel. Other types of structures with different terminating layers of the substrate or more advanced treatment of the polar property of the ferroelectric substrate can possibly lead to a moderate but sufficient coupling strengths. Exploring these possibilities is left for future work.

ACKNOWLEDGMENTS

We thank S. Coh and A. Kemper for useful discussions. S. J. and Y. W. are partially funded by the University of Tennessee's Science Alliance Joint Directed Research and Development (JDRD) program, a collaboration with Oak Ridge National Laboratory. A. L. was supported by Grant DE-FG02-05ER46236. A portion of this research was conducted at the Center for Nanophase Materials Sciences, which is a Department of Energy (DOE) Office of Science User Facility. This research used computational resources supported by the University of Tennessee and Oak Ridge National Laboratory's Joint Institute for Computational Sciences and resources of the National Energy Research Scientific Computing Center (NERSC), a DOE Office of Science User Facility.

¹ Q.-Y. Wang, L. Zhi, Z. Wen-Hao, Z. Zuo-Cheng, Z. Jin-Song, L. Wei, D. Hao, O. Yun-Bo, D. Peng, C. Kai, W. Jing, S. Can-Li, H. Ke, J. Jin-Feng, J. Shuai-Hua, W. Ya-Yu, W. Li-Li, C. Xi, X.-C. Ma, and Q.-K. Xue, *Chin. Phys. Lett.* **29**, 037402 (2012).

² Y. Kamihara, T. Watanabe, M. Hirano, and H. Hosono, *J. Am. Chem. Soc.* **130**, 3296 (2008).

³ D. Liu, W. Zhang, D. Mou, J. He, Y.-B. Ou, Q.-Y. Wang, Z. Li, L. Wang, L. Zhao, S. He, Y. Peng, X. Liu, C. Chen, L. Yu, G. Liu, X. Dong, J. Zhang, C. Chen, Z. Xu, J. Hu, X. Chen, X. Ma, Q. Xue, and X. Zhou, *Nat. Commun.* **3**, 931 (2012).

⁴ S. He, J. He, W. Zhang, L. Zhao, D. Liu, X. Liu, D. Mou, Y.-B. Ou, Q.-Y. Wang, Z. Li, *et al.*, *Nat. Mater.* **12**, 605

- (2013).
- ⁵ S. Tan, Y. Zhang, M. Xia, Z. Ye, F. Chen, X. Xie, R. Peng, D. Xu, Q. Fan, H. Xu, J. Jiang, T. Zhang, X. Lai, T. Xiang, J. Hu, B. Xie, and D. Feng, *Nat. Mater.* **12**, 634 (2013).
 - ⁶ J. J. Lee, F. T. Schmitt, R. G. Moore, S. Johnston, Y.-T. Cui, W. Li, M. Yi, Z. K. Liu, M. Hashimoto, Y. Zhang, D. H. Lu, T. P. Devereaux, D.-H. Lee, and Z.-X. Shen, *Nature* **515**, 245 (2014).
 - ⁷ W.-H. Zhang, Y. Sun, J.-S. Zhang, F.-S. Li, M.-H. Guo, Y.-F. Zhao, H.-M. Zhang, J.-P. Peng, Y. Xing, H.-C. Wang, F. Takeshi, H. Akihiko, Z. Li, H. Ding, C.-J. Tang, M. Wang, Q.-Y. Wang, K. He, S.-H. Ji, X. Chen, J.-F. Wang, Z.-C. Xia, L. Li, Y.-Y. Wang, J. Wang, L.-L. Wang, M.-W. Chen, Q.-K. Xue, and X.-C. Ma, *Chin. Phys. Lett.* **31**, 017401 (2014).
 - ⁸ Y. Sun, W. Zhang, Y. Xing, F. Li, Y. Zhao, Z. Xia, L. Wang, X. Ma, Q.-K. Xue, and J. Wang, *Sci. Rep.* **4**, 6040 (2014).
 - ⁹ L. Z. Deng, B. Lv, Z. Wu, Y. Y. Xue, W. H. Zhang, F. S. Li, L. L. Wang, X. C. Ma, Q. K. Xue, and C. W. Chu, *Phys. Rev. B* **90**, 214513 (2014).
 - ¹⁰ J.-F. Ge, Z.-L. Liu, C. Liu, C.-L. Gao, D. Qian, Q.-K. Xue, Y. Liu, and J.-F. Jia, *Nat. Mater.* **14**, 285 (2014).
 - ¹¹ F.-C. Hsu, J.-Y. Luo, K.-W. Yeh, T.-K. Chen, T.-W. Huang, P. M. Wu, Y.-C. Lee, Y.-L. Huang, Y.-Y. Chu, D.-C. Yan, and M.-K. Wu, *Proc. Natl. Acad. Sci.* **105**, 14262 (2008).
 - ¹² P. J. Hirschfeld, M. M. Korshunov, and I. I. Mazin, *Rep. Prog. Phys.* **74**, 124508 (2011).
 - ¹³ A. Chubukov, *Annu. Rev. Condens. Matter Phys.* **3**, 57 (2012).
 - ¹⁴ R. Peng, H. C. Xu, S. Y. Tan, H. Y. Cao, M. Xia, X. P. Shen, Z. C. Huang, C. Wen, Q. Song, T. Zhang, B. Xie, X. Gong, and D. Feng, *Nat. Commun.* **5**, 5044 (2014).
 - ¹⁵ G. Zhou, D. Zhang, C. Liu, C. Tang, X. Wang, Z. Li, C. Song, S. Ji, K. He, L. Wang, *et al.*, arXiv:1512.01948 (2015).
 - ¹⁶ P. Zhang, X.-L. Peng, T. Qian, P. Richard, X. Shi, J.-Z. Ma, B.-B. Fu, Y.-L. Guo, Z. Han, S. Wang, *et al.*, arXiv:1512.01949 (2015).
 - ¹⁷ R. Peng, X. Shen, X. Xie, H. Xu, S. Tan, M. Xia, T. Zhang, H. Cao, X. Gong, J. Hu, B. Xie, and D. Feng, *Phys. Rev. Lett.* **112**, 107001 (2014).
 - ¹⁸ I. I. Mazin, D. J. Singh, M. D. Johannes, and M. H. Du, *Phys. Rev. Lett.* **101**, 057003 (2008).
 - ¹⁹ I. I. Mazin, *Phys. Rev. B* **84**, 024529 (2011).
 - ²⁰ Y. Bang, *New J. Phys.* **16**, 023029 (2014).
 - ²¹ X. Chen, S. Maiti, A. Linscheid, and P. J. Hirschfeld, *Phys. Rev. B* **92**, 224514 (2015).
 - ²² S. Coh, M. L. Cohen, and S. G. Louie, *New J. Phys.* **17**, 073027 (2015).
 - ²³ D.-H. Lee, *Chin. Phys. B.* **24**, 117405 (2015).
 - ²⁴ L. Rademaker, Y. Wang, T. Berlijn, and S. Johnston, arXiv:1507.03967 (2015).
 - ²⁵ Z.-X. Li, F. Wang, H. Yao, and D.-H. Lee, arXiv:1512.06179 (2015).
 - ²⁶ B. Li, Z. W. Xing, G. Q. Huang, and D. Y. Xing, *J. Appl. Phys.* **115**, 193907 (2014).
 - ²⁷ Z. Li, J.-P. Peng, H.-M. Zhang, W.-H. Zhang, H. Ding, P. Deng, K. Chang, C.-L. Song, S.-H. Ji, L. Wang, K. He, X. Chen, Q.-K. Xue, and X.-C. Ma, *J. Phys.: Condens. Matter* **26**, 265002 (2014).
 - ²⁸ J. Bang, Z. Li, Y. Y. Sun, A. Samanta, Y. Y. Zhang, W. Zhang, L. Wang, X. Chen, X. Ma, Q.-K. Xue, and S. B. Zhang, *Phys. Rev. B* **87**, 220503 (2013).
 - ²⁹ P. Giannozzi, S. Baroni, N. Bonini, M. Calandra, R. Car, C. Cavazzoni, D. Ceresoli, G. L. Chiarotti, M. Cococcioni, I. Dabo, A. D. Corso, S. de Gironcoli, S. Fabris, G. Fratesi, R. Gebauer, U. Gerstmann, C. Gougoussis, A. Kokalj, M. Lazzeri, L. Martin-Samos, N. Marzari, F. Mauri, R. Mazzarello, S. Paolini, A. Pasquarello, L. Paulatto, C. Sbraccia, S. Scandolo, G. Sclauzero, A. P. Seitsonen, A. Smogunov, P. Umari, and R. M. Wentzcovitch, *J. Phys.: Condens. Matter* **21**, 395502 (2009).
 - ³⁰ J. P. Perdew, K. Burke, and M. Ernzerhof, *Phys. Rev. Lett.* **77**, 3865 (1996).
 - ³¹ S. Baroni, S. de Gironcoli, A. Dal Corso, and P. Giannozzi, *Rev. Mod. Phys.* **73**, 515 (2001).
 - ³² X. Gonze and C. Lee, *Phys. Rev. B* **55**, 10355 (1997).
 - ³³ M. Calandra and F. Mauri, *Phys. Rev. B* **71**, 064501 (2005).
 - ³⁴ F. Giustino, M. L. Cohen, and S. G. Louie, *Phys. Rev. B* **76**, 165108 (2007).
 - ³⁵ J. Noffsinger, F. Giustino, B. D. Malone, C.-H. Park, S. G. Louie, and M. L. Cohen, *Comput. Phys. Commun.* **181**, 2140 (2010).
 - ³⁶ M. Calandra, G. Profeta, and F. Mauri, *Phys. Rev. B* **82**, 165111 (2010).
 - ³⁷ M. Wierzbowska, S. de Gironcoli, and P. Giannozzi, arXiv:cond-mat/0504077 (2005).
 - ³⁸ M. Kawamura, Y. Gohda, and S. Tsuneyuki, *Phys. Rev. B* **89**, 094515 (2014).
 - ³⁹ J. Sjakste, N. Vast, M. Calandra, and F. Mauri, *Phys. Rev. B* **92**, 054307 (2015).
 - ⁴⁰ C. Verdi and F. Giustino, *Phys. Rev. Lett.* **115**, 176401 (2015).
 - ⁴¹ Y. Xie, H.-Y. Cao, Y. Zhou, S. Chen, H. Xiang, and X.-G. Gong, *Sci. Rep.* **5**, 10011 (2015).
 - ⁴² G. Grimvall, *The Electron-Phonon Interaction in Metals* (North-Holland, Amsterdam, 1981).
 - ⁴³ H. Krakauer, W. E. Pickett, and R. E. Cohen, *Phys. Rev. B* **47**, 1002 (1993).
 - ⁴⁴ D. Kasinathan, J. Kuneš, A. Lazicki, H. Rosner, C. S. Yoo, R. T. Scalettar, and W. E. Pickett, *Phys. Rev. Lett.* **96**, 047004 (2006).
 - ⁴⁵ In the $N \rightarrow \infty$, $\eta \rightarrow 0$ limit, $\xi(\mathbf{q})$ diverges at $\mathbf{q} = 0$ but is integrable over \mathbf{q} at the same limit, so the total EPC λ with the double delta-function approximation is still well defined, while $\xi(\mathbf{q}, \omega_{\nu\mathbf{q}}) \rightarrow 0$.
 - ⁴⁶ M. L. Kulić and R. Zeyher, *Phys. Rev. B* **49**, 4395 (1994).
 - ⁴⁷ Z. B. Huang, W. Hanke, E. Arrighoni, and D. J. Scalapino, *Phys. Rev. B* **68**, 220507 (2003).
 - ⁴⁸ L. Pietronero, S. Strässler, and C. Grimaldi, *Phys. Rev. B* **52**, 10516 (1995).
 - ⁴⁹ C. Grimaldi, L. Pietronero, and S. Strässler, *Phys. Rev. B* **52**, 10530 (1995).
 - ⁵⁰ V. N. Kostur and B. Mitrović, *Phys. Rev. B* **50**, 12774 (1994).
 - ⁵¹ T. Sohier, M. Calandra, and F. Mauri, *Phys. Rev. B* **91**, 165428 (2015).
 - ⁵² F. Li, Q. Zhang, C. Tang, C. Liu, J. Shi, C. Nie, G. Zhou, Z. Li, W. Zhang, C.-L. Song, *et al.*, arXiv:1512.05203 (2015).
 - ⁵³ J. Shiogai, Y. Ito, T. Mitsushashi, T. Nojima, and A. Tsukazaki, *Nat. Phys.* (2015), 10.1038/nphys3530.
 - ⁵⁴ K. Hanzawa, H. Sato, H. Hiramatsu, T. Kamiya, and H. Hosono, arXiv:1508.07689 (2015).

- ⁵⁵ B. Lei, J. Cui, Z. Xiang, C. Shang, N. Wang, G. Ye, X. Luo, T. Wu, Z. Sun, and X. Chen, arXiv:1509.00620 (2015).
- ⁵⁶ Y. Miyata, K. Nakayama, K. Sugawara, T. Sato, and T. Takahashi, *Nat. Mater.* **14**, 775 (2015).
- ⁵⁷ C.-L. Song, H.-M. Zhang, Y. Zhong, X.-P. Hu, S.-H. Ji, L. Wang, K. He, X.-C. Ma, and Q.-K. Xue, arXiv:1511.02007 (2015).
- ⁵⁸ J. Seo, B. Kim, B. Kim, J. Jeong, J. Ok, J. Kim, J. Denlinger, C. Kim, and Y. Kim, arXiv:1511.07950 (2015).
- ⁵⁹ Z. Ye, C. Zhang, H. Ning, W. Li, L. Chen, T. Jia, M. Hashimoto, D. Lu, Z.-X. Shen, and Y. Zhang, arXiv:1512.02526 (2015).